JOURNAL OF SPACECRAFT AND ROCKETS
Vol. 40, No. 2, March–April 2003

Numerical Prediction of Laminar Shock/Shock Interactions in Hypersonic Flow

Domenic D'Ambrosio[*]
Politecnico di Torino, 10129 Turin, Italy

Results are presented of a series of numerical simulations of experiments conducted at the ONERA Chalais-Meudon Research Center and at the Calspan—University at Buffalo Research Center on shock/shock interactions. The flowfield characteristics are described with the aid of the numerical predictions, and the computed values of surface pressure and heat transfer are compared with the experimental measurements for purposes of verification and validation. Issues related to boundary conditions, grid convergence, and time unsteadiness of the computational fluid dynamics simulations are addressed, and the difficulties that characterize the validation of the computational results are put in evidence.

Nomenclature

$\boldsymbol{F}$ = flux vector
h = enthalpy, J/kg
M = Mach number
$\boldsymbol{n}$ = normal unit vector
p = pressure, Pa
R = radius, reference length, m
Re = Reynolds number
$\mathcal{S}$ = surface, m^2
T = temperature, K
t = time, s
$\boldsymbol{U}$ = primitive variables vector
u, v = velocity components in the x and y directions, m/s
V = velocity, m/s
$\mathcal{V}$ = volume, m^3
$\boldsymbol{W}$ = conservative variables vector
X = axis oriented in the direction between two cells
x, y = Cartesian body axes, m
Δn = distance from the wall of the first cell center, m
θ = angular measurement, deg
μ = dynamic viscosity, kg/m · s
ρ = density, $\mathrm{kg/m}^3$

Subscripts

c = cell
cyl = cylinder
I = inviscid
t = time derivative
V = viscous
w = wall conditions
X = space derivative
∞ = freestream conditions

Superscript

0 = stagnation conditions

Introduction

THE correct evaluation of the heating loads produced by shock/shock interactions represents a critical problem in the design of hypersonic vehicles. In case of airbreathing propulsion, the phenomenon is typically located at the intake cowl lip, where the shocks produced by the compression ramps intersect the bow shock ahead of the cowl, but in general it may affect in a similar manner the wing or the fin leading edge also.

In the past few years, some experimental campaigns have been conducted with the aim of better understanding the phenomenon and of providing data for code validation. In fact, even though the computational fluid dynamics (CFD) is widely used today in the prediction of hypersonic flows for design purposes, noticeable efforts are still necessary to assess the capability and the credibility of CFD codes to deal with the complex physics and multiple length scales.[1,2]

The two most recent sets of experiments on shock/shock interaction were conducted at ONERA Chalais-Meudon, France, in the wind-tunnel R5Ch (Ref. 3) and at Calspan—University at Buffalo Research Center, in the Large Energy National Shock (LENS) tunnel.[4] Subsequently, various numerical simulations have been carried out for reproducing the experimental data, in particular those obtained by ONERA.[5,6] In addition, both the experiments have been selected for validating CFD capability in the framework of the activities of the NATO Research Technology Organization Advanced Vehicle Technology Working Group 10, Subgroup 3, CFD Validation for Hypersonic Flight.[7,8]

In this paper, the results of numerical predictions of both the French and the American experiments will be presented. The paper is organized as follows. In the next section, the flow patterns that characterize the most severe shock/shock interference types will be briefly presented. Then, the model setup and the test conditions of both the ONERA and the CALSPAN experiments will be described. Subsequently, a section will be dedicated to introducing the numerical method that was used to carry out the computations. Finally, the obtained numerical results will be shown and compared with the experimental data. Issues related to boundary conditions, grid convergence, and time unsteadiness of the CFD simulations will be addressed and the difficulties that characterize the validation of the computational results will be put into evidence.

Edney-Type Interactions

Edney-type interactions[9] typically occur when an oblique shock meets a detached shock that forms ahead of a blunt body. Depending on the strength of both the impinging and the bow shocks and on their relative position, various shock interference patterns can occur. In his fundamental work for the study of shock-on-shock interactions, Edney[9] classified six different types of interference. Among them, the third and the fourth ones are the most severe cases, leading to highly localized regions of surface pressure and heat transfer rates on the body downstream of the interaction. Interference types III and IV (Fig. 1) are present when the impinging shock meets the bow shock where it is strong, that is, between the upper and lower sonic lines. Because the two interfering shocks have very different

---

Presented as Paper 2002-0582 at the AIAA 40th Aerospace Sciences Meeting, Reno, NV, 14–17 January 2002; received 8 March 2002; revision received 2 September 2002; accepted for publication 12 November 2002.

[*] Assistant Professor, Department of Aerospace Engineering, Corso Duca degli Abruzzi, 24; domenic@athena.polito.it.

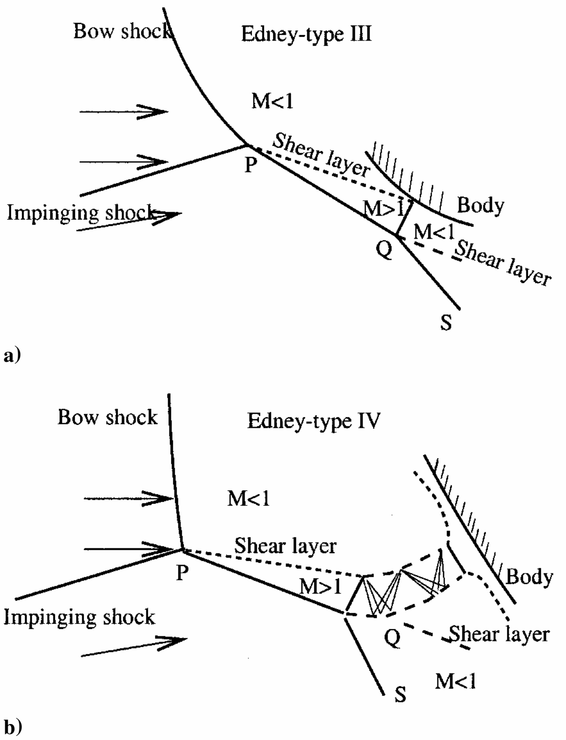

Fig. 1 Edney-type III and IV interactions.[9]

intensities, a shear line is generated that separates a region with subsonic flow from a region where the flow is supersonic. Depending on the angle between the shear layer and the tangent to the body surface and provided that the Mach number in the supersonic region is sufficiently high, it is possible that the shear layer reattaches on the obstacle. This situation corresponds to a type III interference (Fig. 1a). When the inclination of the blunt-body surface with respect to the shear layer is too large, a supersonic jet is formed that is surrounded by a region of subsonic flow. Sometimes, the supersonic jet is too curved and grazes the body surface, but usually it is directed toward the body. In such occasions, the flow experiences a final strong compression across a normal shock at a short distance from the wall (Fig. 1b). The situation is called a type IV interference, and it produces the highest levels of pressure and heat transfer on the body surface.

Model Setup and Test Conditions

ONERA Experiments

The experiments carried out at ONERA in the R5Ch blowdown wind tunnel[3] were characterized by the nominal stagnation and freestream conditions listed in Table 1. The experimental setup that produced an Edney-type IV interaction[9] is shown in Fig. 2. The shock generator, a prism whose cross section is an isosceles triangle with the base 100 mm long and leading-edge angle of 10 deg, has a spanwise dimension of 100 mm. In the present experiments, it was rotated 10 deg with respect to the freestream, so that a wedge/flat plate configuration with 20-deg-wedge angle was obtained. The cylinder, which was placed with its axis perpendicular to the freestream, has a radius of 8 mm. Because its span is 100 mm wide, a two-dimensional flow can be assumed at the middle of the model, where the measurement equipment was mounted. The relative locations of the cylinder and the wedge could be varied to obtain different types of shock/shock interactions. In particular, for the Edney-type IV interference, the distance between the leading edge of the shock generator and the cylinder center was 110 mm along the x axis and 53 mm along the y axis. Two models of the cylinder were built and equipped with pressure taps and thermocouples to measure surface pressure and heat transfer, respectively. In addition, a dual-line coherent anti-Stokes Raman scattering technique was used to perform instantaneous measurements of temperature and density inside the flowfield.

Table 1 Experimental conditions at ONERA

Condition	Value
T^0	1,050 K
p^0	250,000 Pa
T_∞	52.5 K
p_∞	5.9 Pa
M_∞	9.95
Re_∞	$1.66 \times 10^5\ \text{m}^{-1}$
R_{cyl}	0.008 m

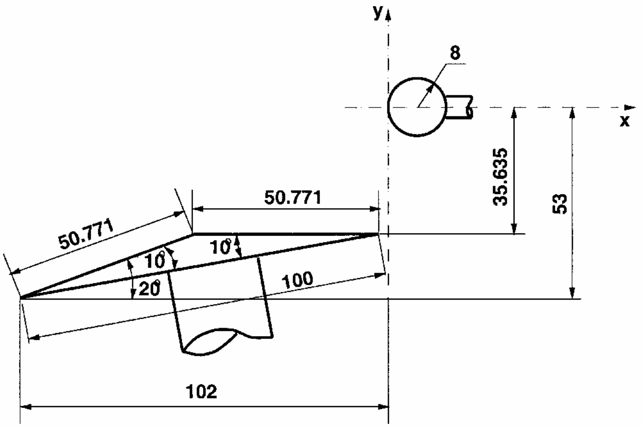

Fig. 2 Model used in ONERA experiments for Edney-type IV interaction[9]; dimensions in millimeters.

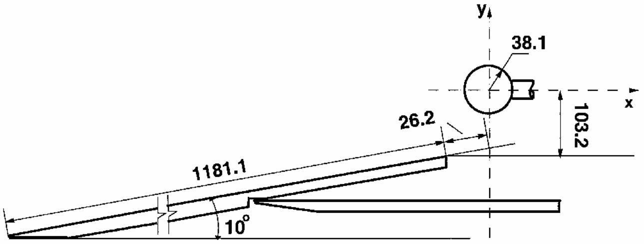

Fig. 3 Model used in the CALSPAN experiments for the Edney type IV interaction[9]; dimensions in millimeters, run 38.

CALSPAN Experiments

Experimental studies were conducted at Calspan in the Veridian 48-in. shock tunnel[4] to obtain detailed heat transfer and pressure measurements in regions of shock/shock interaction in laminar and turbulent low-density flows at Mach numbers from 10 to 16. Seven runs were conducted in the laminar regime, two at Mach 15.7 using a cylinder with radius of 9.525 mm and five at Mach 14 using a cylinder with radius of 38.1 mm. Another seven runs were in the turbulent regime at Mach 10.8, using a cylinder with radius of 38.1 mm. Miniature high-frequency instrumentation was used to resolve the large heat transfer gradients and the flow unsteadiness observed in these studies. To minimize errors in the heat transfer measurements, which may arise from lateral heat conduction effects inside the model in case of large peak heating values, it was preferred to use models with nonconducting surfaces. Then, in those experiments where the resulting wall temperature rises were important, the surface temperature distribution was tabulated together with the heat transfer rate, so that it could be used in future numerical predictions as a boundary condition.[4] The data obtained in the experimental studies have been incorporated in a database called CUBDAT,[10,11] which can be used by researchers involved in numerical prediction studies. In this paper, numerical results related to the conditions of runs 43 and 38 (Fig. 3 and Table 2) of the CUBDAT database will be presented.

Governing Equations

The computational results that will be presented in this paper have been obtained using a numerical technique that integrates in time the

Table 2 Experimental conditions at Calspan for runs 38 and 43

Condition	Run 38	Run 43
T^0, K	3,211.1	3,355.6
p^0, Pa	3,212,957	2,992,325
T_∞, K	100.0	110.
p_∞, Pa	3.66	3.51
$\rho_\infty \times 10^{-4}$, kg/m^3	1.273	1.108
M_∞	14.15	13.94
$Re_\infty \times 10^4$/m	5.2165	4.2618
T_w, K	296.67	300.
R_{cyl}, m	0.0381	0.0381

Navier–Stokes equations for two-dimensional laminar flows. The latter can be written in the following compact conservative form:

$$\frac{\partial}{\partial t}\int_{\mathcal{V}} \boldsymbol{W}\,\mathrm{d}\mathcal{V} + \int_{\mathcal{S}} \boldsymbol{F}_I \cdot \boldsymbol{n}\,\mathrm{d}\mathcal{S} + \int_{\mathcal{S}} \boldsymbol{F}_V \cdot \boldsymbol{n}\,\mathrm{d}\mathcal{S} = 0 \qquad (1)$$

where $\mathcal{V}$ represents an arbitrary volume enclosed in a surface $\mathcal{S}$ with unit normal $\boldsymbol{n}$. Vector $\boldsymbol{W}$ contains the conservative variables and tensors $\boldsymbol{F}_I$ and $\boldsymbol{F}_V$ incorporate the convective (inviscid) fluxes and the diffusive (viscous) fluxes, respectively. The explicit form of $\boldsymbol{W}$, $\boldsymbol{F}_I$, and $\boldsymbol{F}_V$ can be found in any fluid dynamics textbook.

The gas here considered is air, and the hypothesis of perfect gas is assumed. The dynamic viscosity is computed according to classical Sutherland's law, and the thermal conductivity is obtained using the definition of the Prandtl number, whose value is fixed to 0.72.

Numerical Approach

Discretization and Integration in Time

The governing equations are discretized in space by using a cell-centered finite volume approximation over structured meshes. The discretized form of Eq. (1) is given by

$$\frac{\boldsymbol{W}_{I,J}^{K+1} - \boldsymbol{W}_{I,J}^{K}}{\Delta t}\Delta V_{I,J} + \sum_{j=1}^{4}\left(\boldsymbol{F}_I\right)_j \cdot \boldsymbol{n}_j\,\Delta S_j$$
$$+ \sum_{j=1}^{4}(\boldsymbol{F}_V)_j \cdot \boldsymbol{n}_j \Delta S_j = 0 \qquad (2)$$

where superscript K indicates the time level and subscript I, J identifies a cell. The fluxes summation is performed for the four j lateral surfaces that surround the cell. Equation (2) is integrated in time using a forward explicit method:

$$\boldsymbol{W}_{I,J}^{K+1} = \boldsymbol{W}_{I,J}^{K} - \frac{\Delta t}{\Delta V_{I,J}}\left[\sum_{j=1}^{4}(\boldsymbol{F}_I)_j \cdot \boldsymbol{n}_j \Delta S_j + \sum_{j=1}^{4}(\boldsymbol{F}_V)_j \cdot \boldsymbol{n}_j \Delta S_j\right] \qquad (3)$$

where the time step Δt is limited by the Courant–Friedrichs–Lewy condition.

A multiblock domain decomposition method is used to obtain an effective and efficient distribution of grid points across the computational domain.

Evaluation of the Inviscid Fluxes

The inviscid fluxes $(\boldsymbol{F}_I)_j$ at cell interfaces are evaluated using the upwind flux-difference splitting (FDS) Riemann solver proposed in Ref. 12. Upwind methods present the appealing feature of introducing the elements of the wave propagation phenomenology in the integration of the conservation laws. In particular, the adopted FDS technique consists in defining and solving a special initial-value problem, called the Riemann problem (see Ref. 13), at each lateral surface. The Riemann problem, that is, the evolution in time of the flow discontinuities that are present at each lateral surface due to the discretization, is solved here in an approximate way: shock waves that could be generated by the collapse of the initial discontinuities are approximated by compression waves. The conservative form of the equations ensures that the correct jump and entropy conditions are satisfied. The present FDS method[12] is very similar to the popular Osher scheme (see Ref. 14). In fact, it is the mirror image of the latter in the ordering of the partial integration paths.

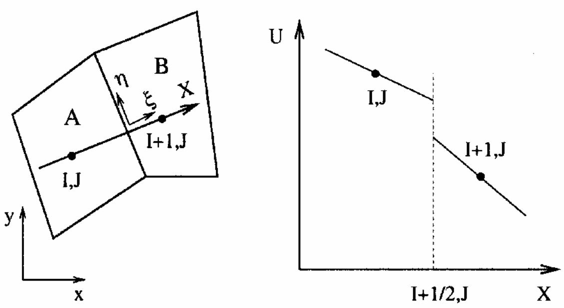

Fig. 4 Linear distribution of initial data.

Evaluation of the Viscous Fluxes

Velocity and temperature gradients needed to evaluate viscous fluxes $(\boldsymbol{F}_V)_j$ in correspondence with lateral surfaces are computed through a standard technique that uses central differences and applies the Gauss divergence theorem.

Second-Order Accuracy

Second-order accuracy in space and time is achieved following the guidelines of the essentially nonoscillatory schemes for shock-capturing techniques,[15] which are capable of avoiding spurious oscillations at flow discontinuities.

In space, a piecewise linear distribution is assumed for the primitive variables $\boldsymbol{U} = \{p, u, v, h\}$ to set the initial conditions for the Riemann problem. The space derivatives of $\boldsymbol{U}$, which are needed to define the linear distribution, are obtained from the space derivatives of the Riemann variables, limited earlier using a minmod operator.

Second-order accuracy in time is reached by computing time derivatives $\boldsymbol{U}_t = \{p_t, u_t, v_t, h_t\}$ through the complete quasi-linear form of the Navier–Stokes equations. The necessary x and y derivatives are obtained through proper rotation of the space derivatives that have already been evaluated for spatial accuracy.

The described spatial and temporal second-order corrections are finally used to update the initial data for the Riemann problem. For instance, with reference to Fig. 4, the left and right initial values across surface $(I + \frac{1}{2}, J)$ can be computed according to the following equations:

$$\left(\boldsymbol{U}_{I+\frac{1}{2},J}\right)_L = \boldsymbol{U}_{I,J} + (\boldsymbol{U}_X)_{I,J}(\Delta X_{A-B}/2) + (\boldsymbol{U}_t)_{I,J}(\Delta t/2) \qquad (4a)$$

$$\left(\boldsymbol{U}_{I+\frac{1}{2},J}\right)_R = \boldsymbol{U}_{I+1,J} - (\boldsymbol{U}_X)_{I+1,J}(\Delta X_{A-B}/2)$$
$$+ (\boldsymbol{U}_t)_{I+1,J}(\Delta t/2) \qquad (4b)$$

where ΔX_{A-B} is the distance between the cell centers A and B along X.

Boundary Conditions

No-slip and fixed-temperature conditions are applied at the wall, where pressure is computed solving a half-Riemann problem. Freestream conditions are enforced at the inlet. A zero-gradient assumption is assumed at the exit boundaries for conservative variables.

Numerical Results

Numerical Simulation of the ONERA Experiments

The experiment conducted at the ONERA that produced an Edney-type IV interaction[9] was replicated with a numerical simulation using the freestream conditions listed in Table 3. In this test case, the computation of the flowfield around the shock generator is necessary and it requires particular care. In fact, because of the model setup used (Fig. 2), an intense expansion is generated at the corner between the upstream part of the shock generator, which is a wedge, and the second part, which is a flat plate. The expansion fan bends the oblique shock wave and makes the flow in the

Table 3 Numerical freestream conditions for simulating the ONERA experiment

Condition	Value
p_∞	5.9 Pa
M_∞	9.95
U_∞	1450 m/s
T_∞	52.5 K
ρ_∞	3.910×10^{-4} kg/m^3
μ_∞	3.405×10^{-6} Pa · s
Re_∞	1.66×10^5 m^{-1}
R_{cyl}	0.008 m

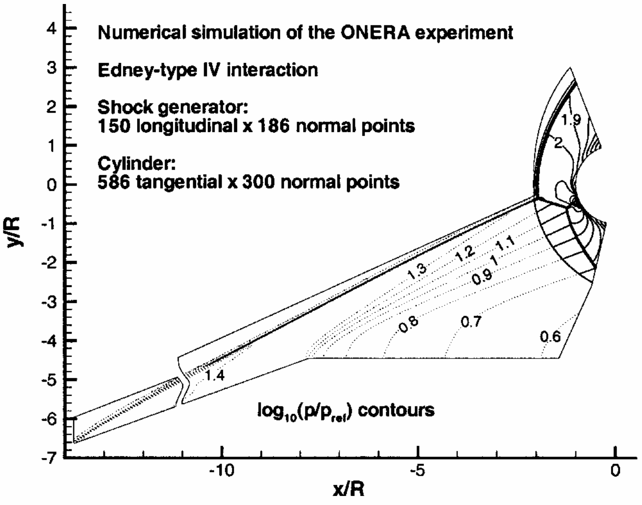

a) Log$_{10}$ of pressure contours

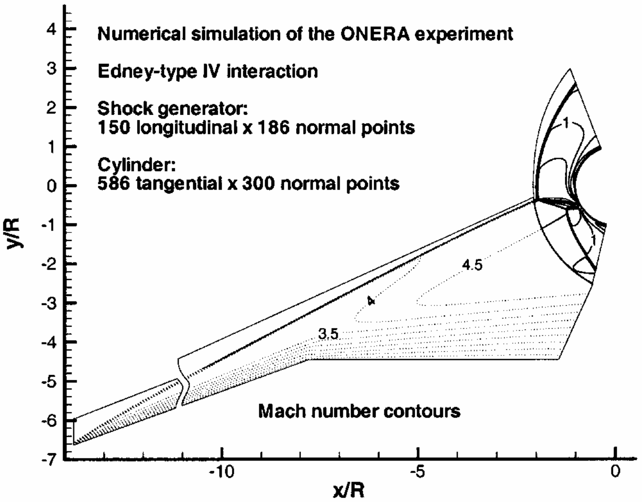

b) Mach number contours

Fig. 5 Simulation of the complete flowfield for the ONERA experiment.

high-pressure side not uniform. In addition, the small size of the cylinder radius with respect to the shock generator characteristic length implies that a slight variation of the inclination (or position) of the impinging shock may produce a noticeable displacement in the position of the stagnation point.

To obtain accurate boundary conditions for the shock interference simulation, the flow around the isolated shock generator was preliminarily computed. The meshes used for such computations were refined both in the normal direction close to the solid walls and also around the oblique shock. In this way, the resolution obtained in capturing the incoming shock was of the same order of magnitude of that of the mesh that would have been subsequently used for computing the shock/shock interaction region. Once the flowfield around the shock generator was computed, the boundary conditions upstream of the cylinder were specified in two different ways. The first method consisted in using overlapping grids when computing the flow around the shock generator and around the cylinder. The two simulations were run uncoupled, and the results around the shock generator were interpolated to the first line of cells of the cylinder grid and used as boundary conditions. The second method exploited the multiblock capability of the CFD code. Here, the shock generator and the cylinder grids were point-matched blocks. Again, the computations around the two objects were run uncoupled, but now it was not necessary to interpolate one solution to another. The simulation of the flowfield around the ONERA experimental setup obtained using the multiblock method is shown in Fig. 5.

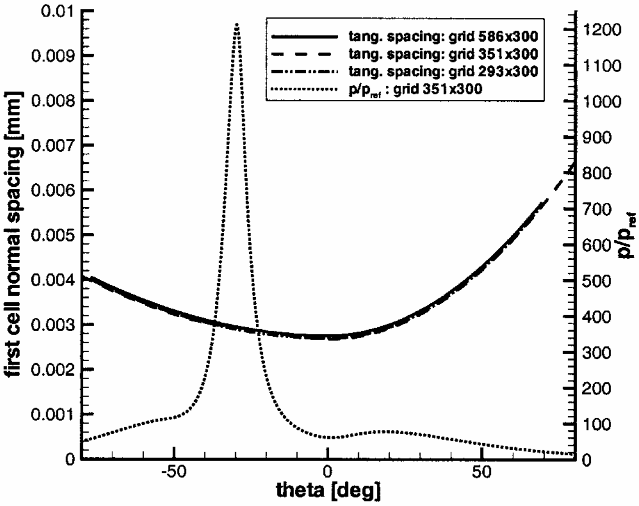

a) Distance of the first cell center from the cylinder wall

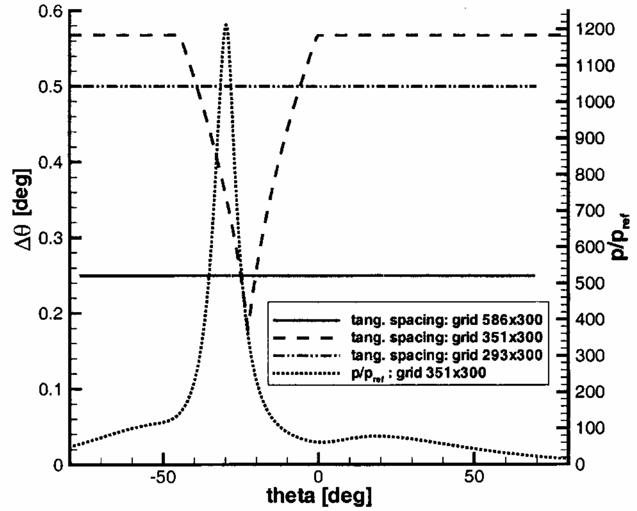

b) Tangential spacing

Fig. 6 Normal and tangential spacing of the grids used to simulate the ONERA experiment.

Globally, five different grids were used to carry out the numerical simulation of the ONERA experiment. The first four grids are composed of 300 points in the direction normal to the body, and they share the same normal spacing. The distance from the wall of the first cell centers (Δn) reaches the minimum value of 2.68 μm in correspondence with $\theta = 0$ ($\Delta n / R_{\text{cyl}} = 3.35 \times 10^{-4}$) and remains below 4 μm along most of the cylinder (Fig. 6a). The minimum cell Reynolds number at the body, $Re_c = \rho_\infty V_\infty \Delta n / \mu_\infty$, is 0.444. However, the tangential spacing varies from one grid to another. When using the first described method for specifying the boundary conditions, two different grids were considered. One grid is characterized by a constant tangential spacing of amplitude $\Delta\theta = 0.57$ deg (310 tangential points), and the other one has a variable tangential spacing that reaches a minimum $\Delta\theta = 0.18$ deg in correspondence with the position $\theta = -22.62$ deg (351 tangential points). When adopting the

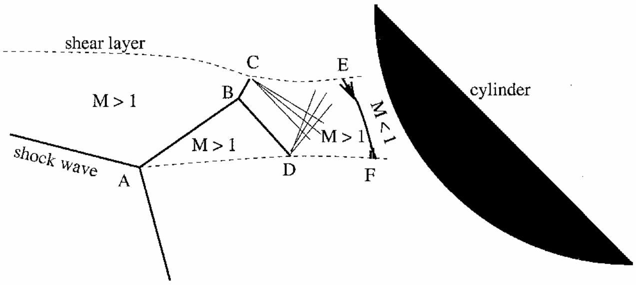

Fig. 7 Wave pattern inside the jet.

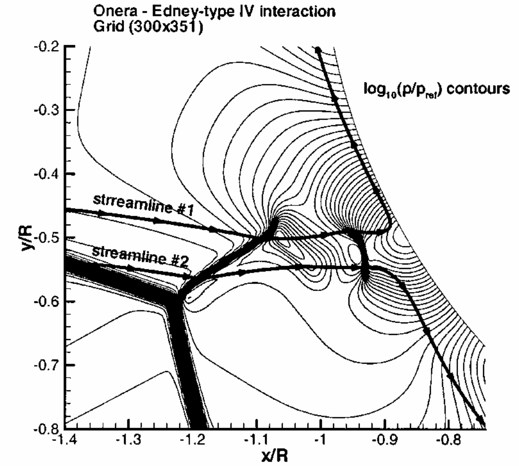

a) Log_{10} of pressure contours

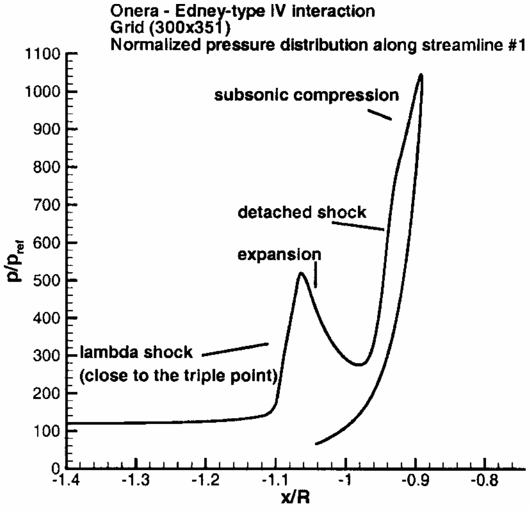

b) Pressure variation along the upper streamline

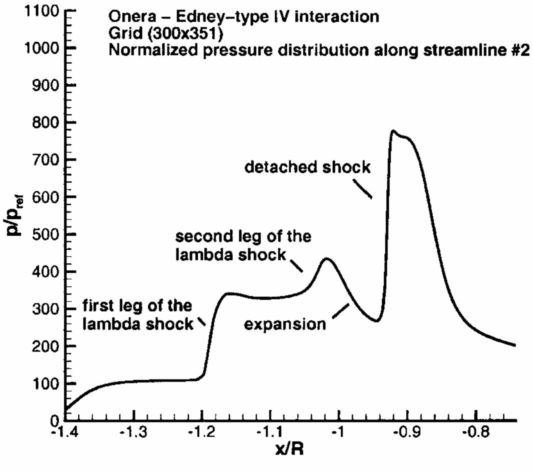

c) Pressure variation along the lower streamline

Fig. 8 Investigation of the wave pattern inside the supersonic jet.

multiblock approach, two grids were also used. The coarsest one has 293 points in the tangential direction, with constant $\Delta\theta = 0.50$ deg. The finest one is composed of 586 points in the tangential direction, with constant $\Delta\theta = 0.25$ deg (Fig. 6b). A fifth mesh was obtained from the latter by eliminating every other grid line in the normal direction (586 × 150 points). In Fig. 6, the mesh spacing data are superimposed to the normalized pressure distribution to show which surface regions require grid refinement.

Before the numerical results obtained using the already described meshes are compared with one another and with the experimental data, the salient features of the computed flowfield will be described. The numerical simulations show that, in the present test case, the shock/shock interference occurs where the bow shock is strong (subsonic flow in the high pressure side). In particular, the interaction belongs to the Edney-type IV family[9] that, as explained before, is characterized by the presence of a supersonic jet surrounded by subsonic flow. In principle, a repeated pattern of expansions and compressions develops inside the jet channel, but here, due to the vicinity of the jet to the cylinder wall, only a few of them are present. From the analysis of the obtained results, the flowfield inside the jet can be interpreted as shown in Fig. 7. The shock wave at the "entrance" the supersonic channel is irregularly reflected from the upper slip line and forms a λ shock. In correspondence with the reflection point, an expansion fan forms to permit parts of the streamlines to flow slightly upward. At the opposite side of the jet, the second leg of the λ shock interacts with the lower slip line and is reflected as an expansion fan, which deviates part of the jet slightly downward. As it approaches the body, the supersonic stream that flows inside the jet is suddenly decelerated through a detached shock. The jet is finally divided in two streams, which flow upward and downward from the stagnation point. The earlier mentioned interpretation arises from the study of Fig. 8, where $\log_{10}$ of the pressure plots are shown in Fig. 8a, with the paths of the two streamlines superimposed. In Figs. 8b and 8c, the pressure distributions along these streamlines are shown. Notice that, after the pressure rise due to the oblique Mach shock, a second increase in pressure, due to the λ shock at the entrance of the channel, is present. This second pressure rise is stronger and unique for the upper streamline, which crosses the λ shock practically at the triple point, while it is less intense, and is followed by a second compression for the lower streamline, which crosses the two legs of the λ shock. Then, both streamlines experience a pressure drop due to the expansion fans and finally a strong compression through the detached shock in front of the body. At this point, particles flow along streamlines 1 and 2 at subsonic speed. Another compression occurs along the upper streamline, while the lower one immediately deviates toward regions at lower pressure.

A larger scale view of the interaction is shown in Fig. 9. Notice that the position of the cylinder bow shock is completely different with respect to the undisturbed case, with the shock layer thickness of the upper portion more than doubled.

Computed pressure and heat flux distributions at the wall are shown in Fig. 10, where the numerical results obtained using the five different grids are compared with the experimental data measured in the ONERA R5Ch low-density wind tunnel.[5] The grid-to-grid comparison shows that a good tangential refinement is necessary to obtain grid-converged peak levels. This can be clearly observed when it is considered that moving the tangential spacing from $\Delta\theta = 0.5$ deg to $\Delta\theta = 0.25$ deg still produces an increase of 7.7% in the pressure peak level and of 14.3% in the heat flux peak. Also the peak location is affected, shifting from about 28 deg with the 293 × 300 mesh to 29.5 deg with the 586 × 300 grid. On the other hand, the normal refinement seems to be less critical. In fact, the pressure and the heat flux peak levels increase just 1.7 and 0.6%, respectively, when passing from the 586 × 150 mesh to the 586 × 300 mesh.

The comparison with the experimental data is rather puzzling. A 37.7% difference can be measured in the pressure peak and even a 50% discrepancy is present in the heat flux peak value. Nevertheless, the measured and computed data are in very good agreement away from the interaction region. With regard to the pressure distribution, the disagreement between the peak levels in the

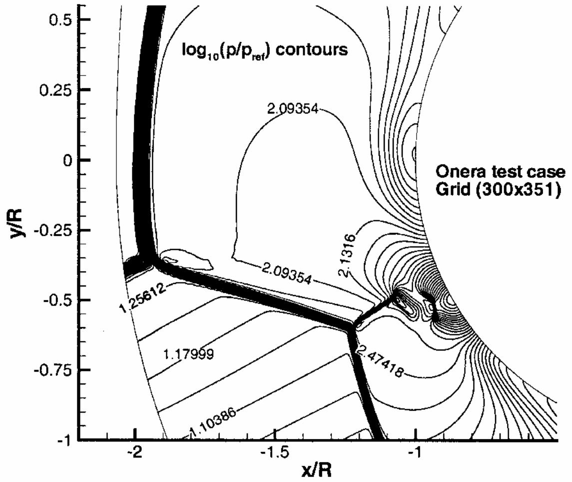

a) Log10 of pressure contours

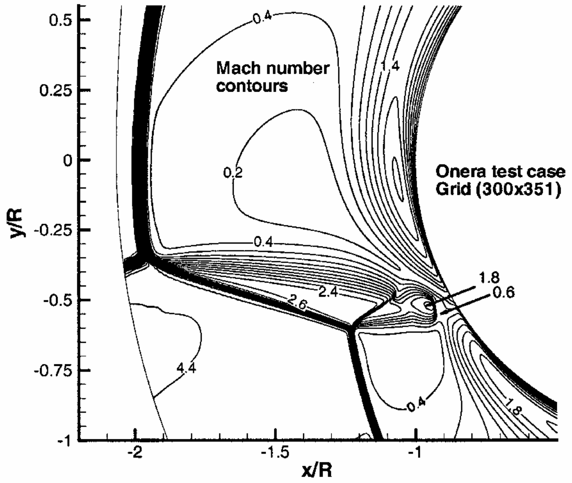

b) Mach number contours

Fig. 9 Interaction region.

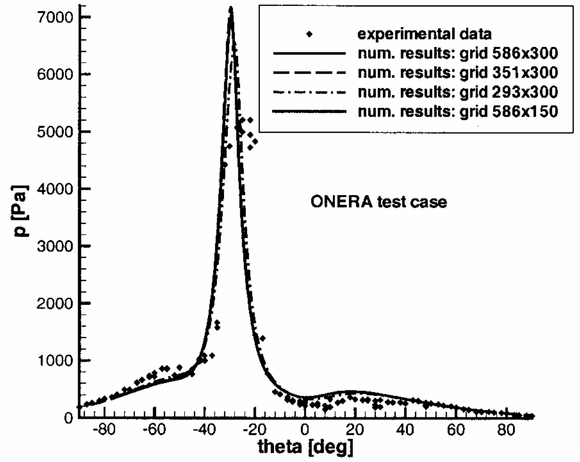

a) Wall pressure distribution

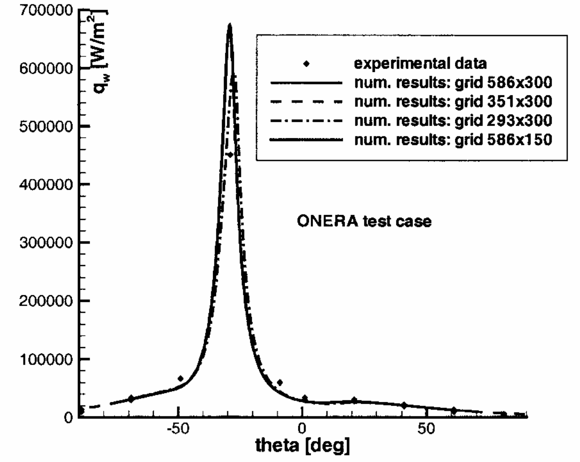

b) Surface heat transfer distribution

Fig. 10 Pressure and heat flux distribution at the wall: experimental values vs numerical predictions.

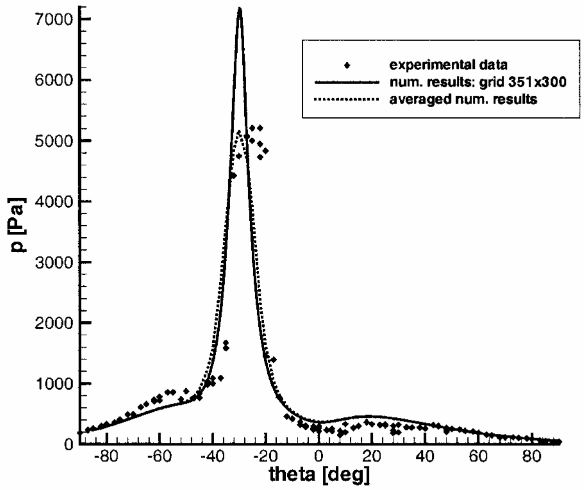

Fig. 11 Pressure distribution at the wall: experimental values vs averaged and not averaged numerical predictions.

numerical simulation and in the experimental measurements could be partially explained with the bad spatial resolution of the experiments, where the diameter of the pressure holes is rather large (1.5 mm).

In the attempt to simulate the smoothing effect of the dimension of the pressure taps on the experimental measurements in the peak region, the numerical data have been averaged out around every experimental measurement point. When the pressure taps with a 1.5 mm diameter are considered, each averaging process involved the cells on the body surface included within an angular range of ±5.37 deg centered in the nominal measurement point. A weighted average has been done to take into account the stretching of the grid in the tangential direction. The results obtained for the surface pressure distribution are very interesting (Fig. 11). In fact, one can see that the peak level is the same when comparing experiments and averaged numerical predictions. However, this result does not explain either the differences that are present immediately below and above the pressure peak, or the different location of the peak itself.

With regard to the differences in the heat flux peak levels, it is impossible to decide whether the isolated experimental point in the peak region represents the maximum heat flux level or not. On the other hand, away from the jet impingement region the experimental and numerical data are in very good agreement.

A general impression that arises from the present comparison between experimental and numerical data is that, for an Edney-type IV interaction,[9] the very narrow physical width of the pressure and heat transfer peaks calls for high accuracy both in the numerical simulation and in the experimental measurements. Thus, on the one hand, it is necessary to use very refined meshes not only in the normal direction and close to the wall, but also and especially in the direction tangential to the body. On the other hand, an adequate refinement level also should be mandatory for the experimental measurements, both in terms of the spacing and of the dimension of the gauges.

Numerical Simulation of CALSPAN Experiments

In this section, numerical results related to the Calspan runs 43 and 38 will be shown and compared with the experimental data. The conditions for the two test cases are listed in Table 2. For both cases, the correct incoming shock position to match with the experiments was obtained by moving the shock until the wall pressure and heat flux peaks were in the same tangential position of the experimental data. The impinging shock strength was computed with the jump conditions for an oblique shock, using the freestream Mach number and the shock-generator angle as input data. This is considered to be an acceptable procedure for simulating the LENS shock/shock interaction experiment.

Because of the relatively high stagnation temperature of these test cases, the choice of the perfect gas model for the computations may be not completely correct. In the experiments, the excited vibrational energy in the reservoir may quickly freeze during expansion in the wind-tunnel nozzle, leading to nonequilibrium freestream conditions. The occurrence of such a phenomenon was recently recognized in the LENS wind tunnel,[16] but it is not accounted for in the present computations.

The numerical simulation of the experimental conditions of run 43 was performed using three different grids. The coarsest grid is composed of 150 points in the normal direction, with grid stretching close to the wall. The distance of the first cell center from the wall, Δn, reaches the minimum value of 24 μm at $\theta = 0$ deg, with $\Delta n/R_{\text{cyl}} = 6.3 \times 10^{-4}$ and $Re_c = 1.025$. In the tangential direction, the grid spacing is 1 deg in the range -40 to $+40$ deg. Then, the tangential grid spacing increases linearly up to a maximum value of 1.5 deg at the upper and lower boundaries, so that the grid dimension is 143×150 points. The second mesh still contains 150 points in the normal direction, but the tangential spacing in the range -40 to $+40$ deg is now 0.5 deg, with maximum amplitude of 1 deg at the ends of the computational domain (263×150 points). For the finest grid, 300 points (with stretching) were used in the normal direction, with a minimum $\Delta n = 12.6\ \mu$m, $\Delta n/R_{\text{cyl}} = 3.31 \times 10^{-4}$ and $Re_c = 0.538$. The tangential spacing is 0.25 deg in the range between -40 and $+40$ deg and then it varies up to the maximum value of 0.5 deg (528×300 points) at $\theta = \pm 90$ deg.

To reproduce the experimental conditions best, the numerical simulations of run 43 were conducted using the wall temperature measured in the experiments as a boundary condition. In addition, to test whether the wall heating has an important effect on the results, two computations were performed using the coarsest grid, with and without the variable wall temperature condition. The comparison between the pressure and heat flux distributions obtained in the two cases[17] showed that, at least in the present conditions, such an effect is definitely negligible.

Run 43 belongs to the family of the Edney-type IV interactions[9] as does the ONERA test case. The Mach number and log$_{10}$ of pressure contours shown in Figs. 12a and 12b clearly reveal the presence of a supersonic jet directed toward the cylinder wall and of a normal shock that decelerates the flow before it reaches the body.

Unlike the ONERA test case, the computations carried out for run 43 using the finest grid were unsteady. To investigate the phenomenon, the simulation was restarted using global time stepping instead of local time stepping. The time evolution of the pressure peak position and level are plotted for a short time interval in Fig. 13. In Fig. 13, time $t = 0$ does not correspond to the moment when the computation was restarted, but it is sufficiently far from it (~0.1 ms) to ensure that possible unphysical oscillations related to the passage from local to global time stepping are no longer present. Within the available time range, it seems to be possible to estimate an oscillation frequency of about 2.5 kHz for the present computation. The result of Fig. 13 is very similar to that obtained by Lind and Lewis[18] in computing an analogous experiment with different freestream conditions. In the present case, the temporal window is definitely shorter than in Ref. 18 because an explicit method is used and because the cells dimensions, which affect the time-step size, are definitely smaller.

Lind and Lewis[18] put the jet unsteadiness in relation to the formation and shedding of a strong vortex that is produced due to the high-velocity gradient across the shear layer that bounds the upper part of the supersonic jet. Nevertheless, such a mechanism was not found in the present computation, where the reason for the unsteady behavior remains unclear.

Wall pressure and heat flux distributions at different instants are shown in Fig. 14 together with the experimental measurements taken from the CUBDAT database.[11] Figures 14a and 14b should be observed with the aid of Fig. 13. The distribution curves are very close to one another, and they may appear confusing, but in fact they show that the peaks can shift of a not negligible distance in a very short time. This raises a question about temporal averaging the experimental data may have undergone. The importance of using instrumentation with high-frequency response for measuring pressure and heat transfer in this kind of flow is stressed in Ref. 4. There, it is reported that instrumentation capable of following frequencies at least in the 30-kHz range must be used to measure accurately

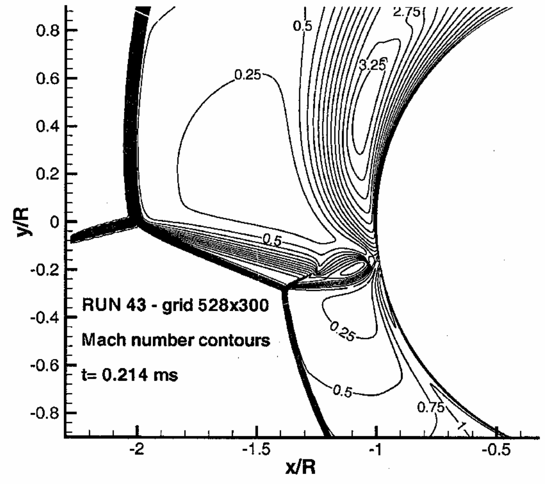

a) Mach number contours

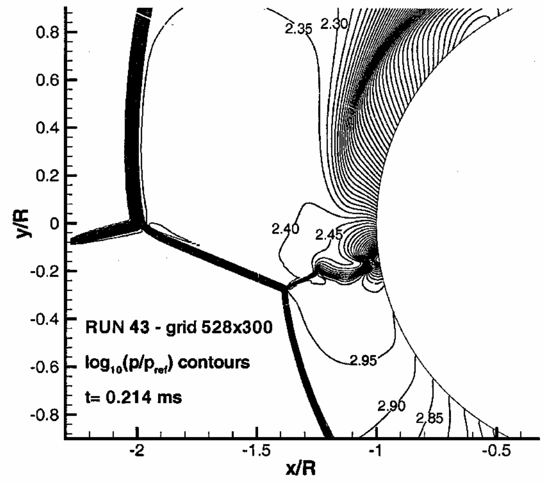

b) Log$_{10}$ of pressure contours

Fig. 12 Mach number and log$_{10}$ of pressure for run 43.

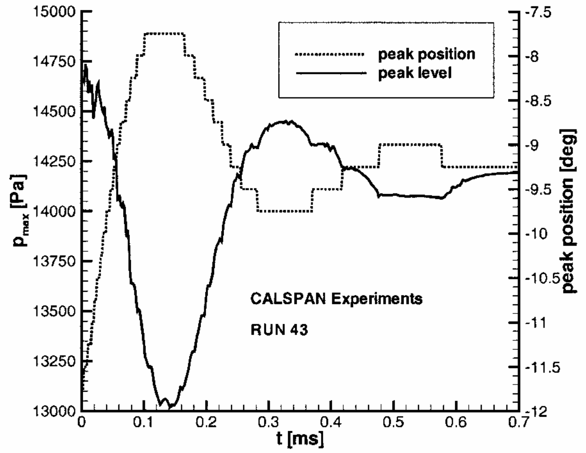

Fig. 13 Time history of the pressure peak position and level for run 43, computed using the 528 × 300 grid.

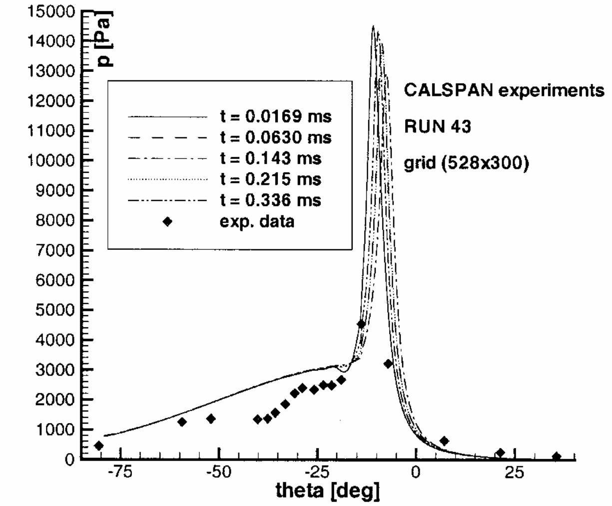

a) Surface pressure distribution

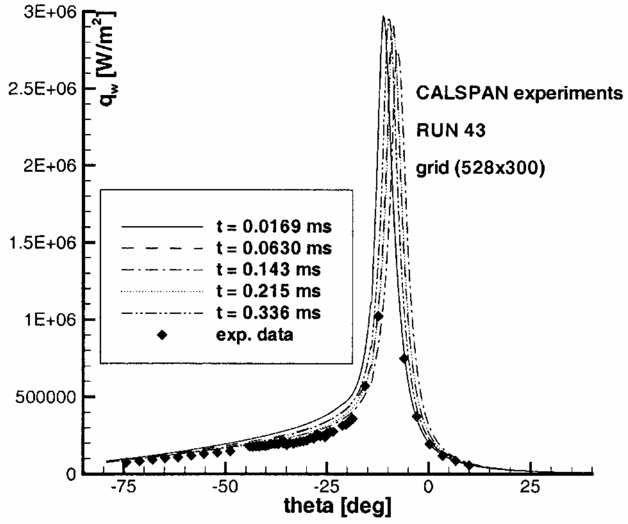

b) Surface heat transfer distribution

Fig. 14 Computed surface pressure and heat flux distributions at different moments; run 43, 528 × 300 grid.

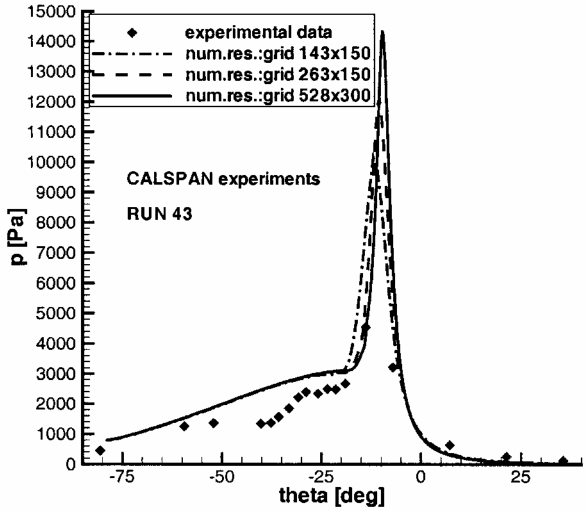

a) Surface pressure distribution

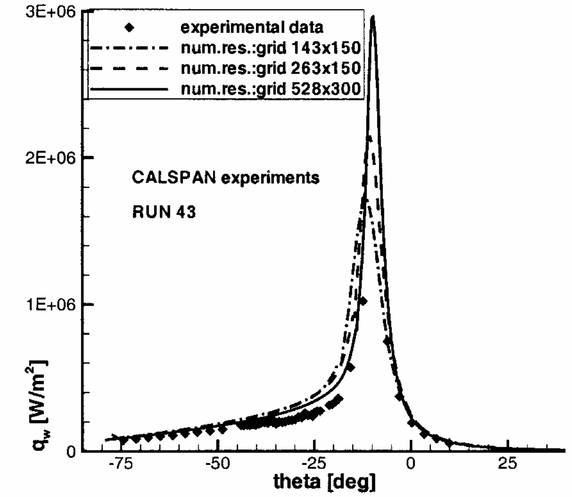

b) Surface heat transfer distribution

Fig. 15 Pressure and heat flux distribution at the wall for run 43: experimental values vs numerical predictions.

surface distributions. Information about the temporal resolution and history of the experimental measurements is fundamental for code validation purposes. For instance, considering the heat flux distributions of Fig. 14b, it is possible to see that, at least in one instant, each experimental point is close to one of the computed curves. Unfortunately, this does not prove that the numerical results are correct because the temporal variation of the experimental data is not known to the author.

Despite the not too bad agreement with the heat flux measurements, the comparison between the experimental and the numerical wall pressure distribution is not satisfactory at all. First, as well as for the heat flux measurements, the spatial resolution of the experimental data is too coarse to provide useful information about the peak value. Second, the differences along the wings of the peak value are too large and unaccountable, in particular on the left side (Fig. 14a). In this connection, note that exactly the same results[8] for the off-peak values were computed by Candler and Boyd (see Ref. 8) the latter using a direct simulation Monte Carlo method.

A grid-to-grid comparison is shown in Figs. 15a and 15b. The results related to the finest grid (528 × 300), which are unsteady, are recorded at time $t = 0.336$ ms. Figures 15a and 15b confirm the that the pressure and heat flux peaks thinness requires a strong tangential grid refinement before grid convergence is achieved. In the case shown in Fig. 15, for instance, the increments of the pressure and heat flux peak values are, respectively, of 19 and 23% when passing from the 143 × 150 grid to the 263 × 150 grid and of 19 and 40% when passing from the 263 × 150 grid to the 528 × 300 grid. In the latter case, the increase should be partially due to the normal refinement, but, according to the lesson learned in simulating the ONERA test case, the largest effect is to be attributed to the improved tangential spacing.

The last test case considered here is Calspan run 38. The numerical investigation was performed using two different grids. The coarsest grid is composed of 75 points in the normal direction (minimum $\Delta n = 38.7$ μm, $\Delta n/R_{\mathrm{cyl}} = 1.01 \times 10^{-3}$, and $Re_c = 2.010$), with a constant spacing of 1 deg in the tangential direction. The finest one has 250 points normal to the wall (minimum $\Delta n = 14.9$ μm, $\Delta n/R_{\mathrm{cyl}} = 3.91 \times 10^{-4}$, and $Re_c = 0.777$) and the constant tangential spacing is 0.5 deg. The numerical results show that the shock interaction occurring in run 38 is an Edney-type[9] IV. No sign of unsteadiness was detected in this case. Although acquired experience suggests that the normal refinement of the finest grid should be sufficient, it also makes it clear that the tangential mesh refinement is still inadequate to claim grid convergence in the peak region. The reason for showing these computations here (Fig. 16), however, is that they put in evidence again the strong discrepancy between numerical results and experimental measurements that is also present in the off-peak values. It is interesting that numerical data obtained by Candler on run 38 and presented in Ref. 8 fully confirm the present numerical results.

The inexplicable differences between experimental and numerical off-peak pressure and heat transfer values are an open question. Because the flow around the shock generator was not computed in both the present numerical simulations and in those included in

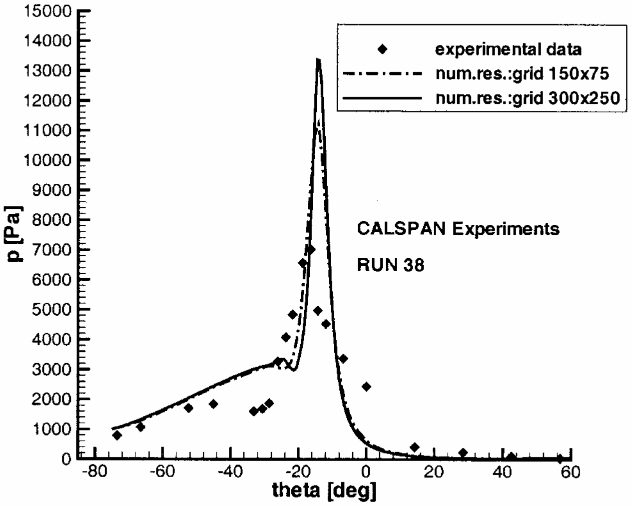

a) Surface pressure distribution

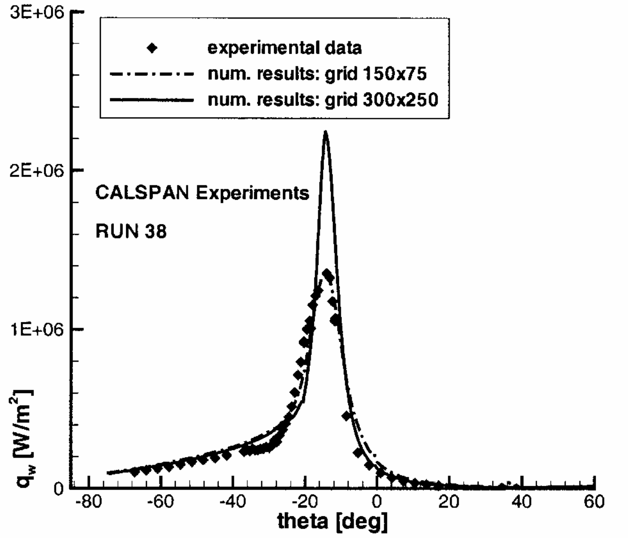

b) Surface heat transfer distribution

Fig. 16 Pressure and heat flux distribution at the wall for run 38: experimental values vs numerical predictions.

Ref. 8, a reasonable suggestion for a future investigation is to replicate numerically the entire experimental setup, or at least to check whether the hypersonic viscous interaction on the ramp noticeably changes the post-impinging shock conditions with respect to those obtained using the Rankine–Hugoniot relations. If the impinging shock intensity does change, then the boundary conditions used by the author and by Candler and Boyd in the results appearing in Ref. 8 do not exactly replicate the experimental conditions and thus a computation of the complete experimental setup is necessary. Another possible source of discrepancy could be that the impinging shock was not completely steady during the experiment. In fact, small fluctuations in the flow at the exit of the wind-tunnel nozzle may produce not negligible oscillations both in the strength of the impinging shock and in the position of the impinging point, which is about 1 m away from the wedge leading edge.

Conclusions

The numerical investigation on shock/shock interactions has put in evidence some of the major difficulties that can be encountered in computational simulation of such kind of flows.

The first issue concerns the strong tangential grid refinement that is necessary to capture accurately the very narrow pressure and heat flux peaks that are present where the jet impinges on the wall. Such a resolution problem is also common to experimental measurements. Often, in fact, the physical width of the peaks is so narrow that it can not be captured in an experimental setup.

The second issue is related to the use of the correct boundary conditions in the numerical simulation of the shock/shock interaction. Sometimes, in fact, the experimental setup is such that imposing the Rankine–Hugoniot relations for evaluating the impinging shock strength is an inadequate procedure. In this work, the Calspan experiments were simulated using these relations, but the low density of the freestream conditions leaves some doubt about the possible influence of hypersonic viscous interaction on the impinging shock characteristics. Numerical simulations including the shock-generator flowfield will be the object of future work.

A third problem is connected to the unsteady behavior that sometimes characterize the Edney-type IV interactions.[9] The unsteadiness could be due both to an inherent time-dependent character of the supersonic jet (fed by some kind of feedback mechanism in the subsonic portion of the bow shock) and to the presence of disturbances in the wind-tunnel flow. In any case, the numerical simulation must be time accurate, and the experimental instrumentation must be characterized by a high-frequency response. For validation purposes, detailed information about the time evolution of the experimental measurements and about the experiment startup should be available.

References

[1] Metha, U. B., "Credible Computational Fluid Dynamics Simulations," *AIAA Journal*, Vol. 36, No. 5, 1998, pp. 665–667.

[2] Rizzi, A., and Vos, J., "Toward Establishing Credibility in Computational Fluid Dynamics Simulations," *AIAA Journal*, Vol. 36, No. 5, 1998, pp. 668–675.

[3] Pot, T., Chanetz, B., Lefebvre, M., and Bouchardy, P., "Fundamental Study of Shock–Shock Interference in Low Density Flow: Flowfield Measurements by DLCARS," ONERA, TP 1998-140, July 1998.

[4] Holden, M., Sweet, S., Kolly, J., and Smolinsky, G., "A Review of the Aerothermal Characteristics of Laminar, Transitional and Turbulent Shock/Shock Interaction Regions in Hypersonic Flows," AIAA Paper 98-0899, Jan. 1998.

[5] Moss, J., Pot, T., Chanetz, B., and Lefebvre, M., "DSMC Simulation of Shock/Shock Interactions: Emphasis on Type IV Interactions," ONERA, TP 1999-107, July 1999.

[6] Glass, C., "Numerical Simulation of Low-Density Shock-Wave Interactions," NASA TM-1999-209358, July 1999.

[7] Knight, D. D., "Overview of RTO WG 10 Subgroup 3," AIAA Paper 2002-0433, June 2002.

[8] Walker, S., and Schmisseur, J., "CFD Validation of Shock-Shock Interaction Flow Fields," AIAA Paper 2002-0436, Jan. 2002.

[9] Edney, B., "Anomalous Heat-Transfer and Pressure Distributions on Blunt Bodies at Hypersonic Speeds in the Presence of an Impinging Shock," Aeronautical Research Inst. of Sweden, FFA Rept. 116, Stockholm, Feb. 1968.

[10] Holden, M., Moselle, J., and Martin, S., "A Database for Aerothermal Measurements in Hypersonic Flow for CFD Validation," AIAA Paper 96-4597, 1996.

[11] "Experimental Database from CUBRC Studies in Hypersonic Laminar and Turbulent Interacting Flows Including Flowfield Chemistry," RTO Code Validation of DSMC and Navier–Stokes Code Validation Studies, Calspan—Univ. at Buffalo Research Center, Buffalo, NY, Dec. 2000.

[12] Pandolfi, M., "Contribution to the Numerical Prediction of Unsteady Flows," *AIAA Journal*, Vol. 22, No. 5, 1983, pp. 602–610.

[13] Toro, E. F., *Riemann Solvers and Numerical Methods for Fluid Dynamics*, Springer-Verlag, Berlin, 1997, pp. 115–157.

[14] Osher, S., and Solomon, F., "Upwind Difference Schemes for Hyperbolic Systems of Conservation Laws," *Mathematics of Computation*, Vol. 38, No. 158, 1982, pp. 339–374.

[15] Harten, A., Engquist, B., Osher, S., and Chakravarthy, S. R., "Uniformly High Order Accurate Essentially Non-Oscillatory Schemes, III," *Journal of Computational Physics*, Vol. 71, No. 2, 1987, pp. 231–303.

[16] Candler, G. V., Nompelis, I., Druguet, M.-C., Holden, M. S., Wadhams, T. P., Boyd, I. D., and Wang, W.-L., "CFD Validation of Hypersonic Flight: Hypersonic Double-Cone Flow Simulations," AIAA Paper 2002-0581, Jan. 2002.

[17] D'Ambrosio, D., "Numerical Prediction of Laminar Shock/Shock Interactions in Hypersonic Flow," AIAA Paper 2002-0582, Jan. 2002.

[18] Lind, C. A., and Lewis, M. J., "Computational Analysis of the Unsteady Type IV Shock Interaction of Blunt Body Flows," *Journal of Propulsion and Power*, Vol. 12, No. 1, 1996, pp. 127–133.

B. Hassan
Associate Editor